

# Noninvasive Thermometer Based on the Zero-Bias Anomaly of a Superconducting Junction for Ultrasensitive Calorimetry

Bayan Karimi\* and Jukka P. Pekola

*QTF Centre of Excellence, Department of Applied Physics, Aalto University School of Science, P.O. Box 13500, 00076 Aalto, Finland*

(Received 24 July 2018; revised manuscript received 15 October 2018; published 20 November 2018)

We present radiofrequency thermometry based on a tunnel junction between a superconductor and proximitized normal metal. It allows operation in a wide range of biasing conditions. We demonstrate that the standard finite-bias quasiparticle tunneling thermometer suffers from large dissipation and loss of sensitivity at low temperatures, whereas thermometry based on a zero-bias anomaly avoids both of these problems. For these reasons, the latter method is suitable down to lower temperatures, here to about 25 mK. Both thermometers are shown to measure the same local temperature of the electrons in the normal metal in the range of their applicability.

DOI: 10.1103/PhysRevApplied.10.054048

## I. INTRODUCTION

Thermometry forms a basis of detecting radiation quanta. As such, detection of radiant heat by a thermometer dates back to 1878 by Langley [1,2]. For measuring energetic quanta, e.g., x-ray photons or radioactive particles, techniques exist for a few decades [3]. As compared, for instance, to observing 6-keV x-ray photons from Mn K $\alpha$  and K $\beta$  events [4], measuring a microwave single photon with about eight orders of magnitude lower energy in the range of 100  $\mu$ eV poses a great challenge [5–7]. The energy resolution  $\delta\epsilon$  of a calorimeter reads  $\delta\epsilon = \sqrt{CG_{\text{th}}S_T}$ , where  $C$  denotes the heat capacity of the absorber,  $G_{\text{th}}$  the thermal conductance to the heat bath, and  $S_T$  stands for temperature noise. Among these parameters,  $S_T$  is directly related to the performance of the thermometer. The challenge is to have a noninvasive thermometer, operating at low enough temperature with noise not exceeding  $S_T \sim 10 \mu\text{K}/\sqrt{\text{Hz}}$  in order to detect typical 1-K microwave photons, e.g., in superconducting quantum circuits [5,8].

Thermometer candidates for nanocalorimetry purposes include basic normal-metal–insulator–superconductor ( $N$ - $I$ - $S$ ) tunnel junction probes [9–11], superconductornormal-metalsuperconductor ( $S$ - $N$ - $S$ ) Josephson junctions [12,13], superconducting quantum interference devices (SQUIDS) [14], current noise in quantum point contacts [15,16], Dayem bridges [17,18], and proximity circuit quantum electrodynamics (QED) probes [19]. The virtue of a  $N$ - $I$ - $S$  junction in a calorimeter is based on its operation in a continuous manner unlike a common switching detector such as a Josephson junction. In this paper, we present

a thermometer in a rf setup with about 10-MHz bandwidth; it is a  $\mathfrak{N}$ - $I$ - $S$  tunnel junction, where by  $\mathfrak{N}$  we denote normal metal influenced by proximity superconductivity [20,21]. The induced gap in  $\mathfrak{N}$  depends exponentially on the distance from the superconductor in the normal metal. In order to make it noninvasive, we monitor the zero-bias anomaly (ZBA) [21–24] of the junction. We present superior performance as compared to a common quasiparticle (QP) tunneling thermometer due to low dissipation and nonvanishing responsivity down to the lowest temperatures.

## II. DESCRIPTION OF THE SYSTEM

The studied setup in this work consists of a small proximitized Cu island coupled to a clean superconducting Al contact and to two tunnel junctions. A schematic illustration of the measurement setup and a scanning electron microscope (SEM) image of sample A are shown in Figs. 1(a) and 1(b), respectively. The contact to the right in Fig. 1(b) is the thermometer junction, the one to the left is an auxiliary tunnel contact (injector), and the one in the middle is a clean superconductor contact. The structure is fabricated on top of an oxidized silicon substrate by electron-beam lithography (EBL) combined with three-angle shadow evaporation. We present data on two samples. In sample A (B), the resistance of the thermometer tunnel junction is  $R_T = 8 \text{ k}\Omega$  ( $20 \text{ k}\Omega$ ) and the clean contact is  $d = 500 \text{ nm}$  ( $1 \mu\text{m}$ ) away from it. The junction area in both samples is  $A \simeq 0.010 \mu\text{m}^2$ , yielding specific resistance  $R_T A = 80 \Omega\mu\text{m}^2$  ( $200 \Omega\mu\text{m}^2$ ) for sample A (B). In both samples, the thickness of the two Al layers [blue color in Fig. 1(b)] is 20 nm for both and 35 nm for Cu (brown).

\*bayan.karimi@aalto.fi

In this paper, we focus on the  $S\text{-}\mathfrak{N}\text{-}I\text{-}S$  configuration, which is used as a rf thermometer. The  $S\text{-}\mathfrak{N}$  clean contact acts as a heat mirror and fixes the electric potential of the island; it is directly grounded at the sample stage. Importantly, this contact induces proximity superconductivity at the thermometer junction. In order to obtain a fast temperature readout, the superconductor lead of the junction is embedded in an  $LC$  resonator, which is connected to input and output rf lines via coupling capacitors  $C_1$  and  $C_2$ , schematically shown in Fig. 1(a). The dc voltage of the

thermometer  $V_{\text{th}}$  is connected to a bias tee and a small parallel resistor fixed at the printed circuit board of the sample box using a resistive thermocoax dc line (not shown in Fig. 1) [8]. The  $LC$  resonator is made of Al with the thickness of 100 nm and is fabricated by EBL and one angle metallization; it is placed on a separate chip.

Using elementary analysis for the circuit in Fig. 1(a), and assuming almost all the signal applied on the left is reflected, the ratio of voltages  $V_1$  and  $V_2$ ,  $s \equiv 2V_2/V_1$ , is given by

$$s(\omega) = -\frac{i2\omega^3 R_L C_1 C_2 L}{\{1 - \omega^2[L(C + C_1 + C_2) + LC_2 R_L/R]\} + i\omega[L/R + R_L C_2 - \omega^2 L(C_1 + C)R_L C_2]}, \quad (1)$$

where  $R$  is the inverse of the differential conductance  $dI/dV$  of the junction and  $R_L = 50 \Omega$  is the transmission-line impedance. For  $R_L/R \ll 1$ , the resonance frequency  $f_0 = \omega_0/2\pi \simeq 640 \text{ MHz}$  is given by  $\omega_0^2 \approx 1/[L(C_1 + C_2 + C)]$ . Then, at resonance,

$$s(\omega_0) = -\frac{2C_1}{C_2} \frac{1}{1 + R_0 dI/dV}, \quad (2)$$

where  $R_0 = (\omega_0^2 R_L C_2^2)^{-1}$ . Thus, for  $dI/dV \rightarrow 0$ ,  $s(\omega_0) \rightarrow -2C_1/C_2$ ; i.e., it obtains the value given by the ratio of the input and output couplings. Measured in dBm referenced to  $P_0 = 1 \text{ mW}$ , we obtain the transmission in the form

$$S_{21}(\omega_0) = {}^{10} \log \left[ \frac{V_1^2 |s(\omega_0)|^2}{4R_L P_0} \right] = S_0 - {}^{20} \log \left( 1 + R_0 \frac{dI}{dV} \right), \quad (3)$$

where  $S_0 = {}^{20} \log[C_1 V_1 / (C_2 \sqrt{R_L P_0})]$  is a constant offset which, in the actual setup, includes also the attenuation and amplification in the lines. For low conductance,  $dI/dV \ll R_0^{-1}$ , we may linearize the relation between  $S_{21}$  and  $dI/dV$  into the form

$$\frac{dI}{dV} = \frac{\ln(10)}{20R_0} [S_0 - S_{21}(\omega_0)]; \quad (4)$$

i.e.,  $S_{21}$  measures the negative of the differential conductance of the junction.

Figure 2 shows the frequency dependence of  $S_{21}$  of sample A, measured between the right and middle contacts of Fig. 1(b), around the resonance frequency  $f_0$ , at the bath temperature  $T = 170 \text{ mK}$  at different bias voltages  $V_{\text{th}}$  of the thermometer. (We use the symbol  $V_{\text{th}}$  interchangeably with  $V$  when we discuss the actual thermometer junction.) In general, the bias voltage determines the differential conductance  $dI/dV$  of the junction in a way to be described later. It is obvious based on the figure that, at large biases, the resonance line becomes wider due to increasing dissipation (larger  $dI/dV$  of the junction). The inset shows an enlargement of similar data taken at  $T = 30 \text{ mK}$ , demonstrating a negative frequency shift of about 200 kHz when

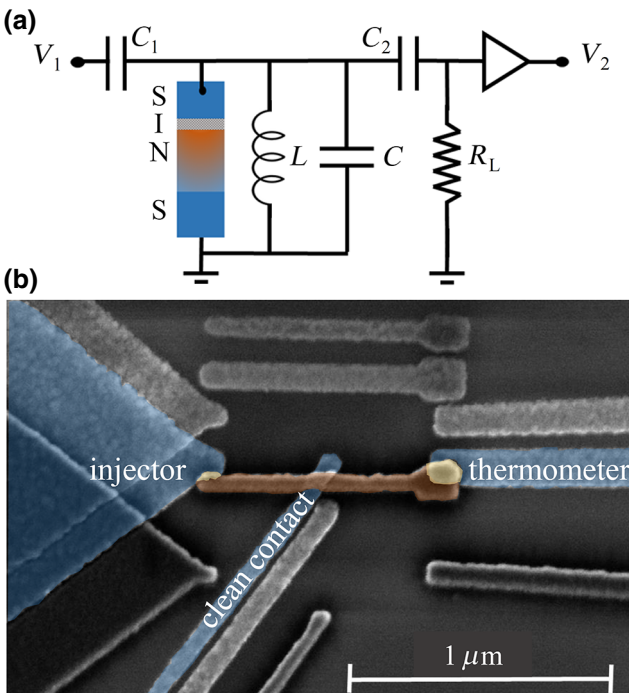


FIG. 1. (a) The studied setup; schematic illustration of the transmission measurement circuit.  $C_1 = 10.3 \text{ fF}$  and  $C_2 = 59.3 \text{ fF}$  are the coupling capacitors,  $C = 0.2 \text{ pF}$  and  $L = 100 \text{ nH}$  the parameters of the  $LC$  resonator, and  $R_L = 50 \Omega$  is the transmission-line impedance. (b) Colored scanning electron micrograph of sample A used in this experiment. A normal metallic island (Cu, brown) is in contact with aluminum leads (blue) either via a clean contact or tunnel barrier (light yellow).

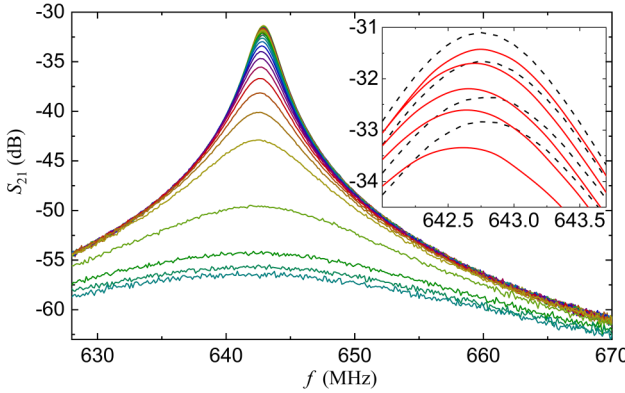


FIG. 2. The transmission  $S_{21}$  measured against the drive frequency  $f$  at  $T = 170$  mK and at  $-120$  dBm power. The different curves with the overall trend from top to bottom correspond to thermometer dc bias voltages  $V_{\text{th}}$  ranging from  $0$  to  $170$   $\mu\text{V}$  in  $5\text{-}\mu\text{V}$  intervals. The inset shows an enlargement of a similar measurement at  $T = 30$  mK, where the dashed curves from bottom to top are for  $V_{\text{th}} = 0, 5, 10, 20$   $\mu\text{V}$  and the solid curves from top to bottom are for  $V_{\text{th}} = 30, 90, 105, 112, 120$   $\mu\text{V}$ . We attribute the tiny frequency shift to finite Josephson inductance.

biasing the junction away from  $V_{\text{th}} = 0$ . This shift is due to the Josephson inductance of the  $\mathfrak{N}$ - $I$ - $S$  junction at zero bias. The Josephson junction with critical current  $I_c$  introduces a parallel to  $L$  inductance  $L_J = \Phi_0/(2\pi I_c)$ , leading to a frequency shift  $\delta f_0/f_0 = L/(2L_J)$  for  $L_J \gg L$ . Here,  $\Phi_0 = h/2e$  is the superconducting flux quantum. The measured frequency shift of about 200 kHz would then imply  $I_c \sim 5$  pA for sample A.

### III. QP THERMOMETRY

Measuring current carried by single electrons (QPs) in an  $N$ - $I$ - $S$  junction has been considered for measurements of power in ultrasensitive nanobolometers [25,26]. For an ideal low-transparency junction biased at voltage  $V$ , the expression for QP current reads

$$I = \frac{1}{2eR_T} \int_{-\infty}^{\infty} dE n_S(E) \{f_N(E - eV) - f_N(E + eV)\}, \quad (5)$$

where  $R_T$  is the resistance of the tunnel junction,  $n_S(E) = |E|/\sqrt{E^2 - \Delta^2}$  the normalized superconducting density of states for  $|E| > \Delta$  and  $n_S(E) = 0$  for  $|E| < \Delta$ , and  $f_N(E) = [1 + \exp(\beta E)]^{-1}$  the Fermi distribution in the normal metal at temperature  $T = (k_B\beta)^{-1}$ . Here,  $\Delta$  denotes the superconducting gap. Far below the critical temperature,  $T \ll T_c$ , and for low biases,  $eV \ll \Delta$ , we have

$$I \approx I_0 e^{-(\Delta - eV)/k_B T}, \quad (6)$$

where  $I_0 = \sqrt{2\pi k_B T \Delta}/(2eR_T)$ . Then, we can combine Eqs. (3) and (6) into

$$T = \frac{\Delta}{k_B} \left(1 - \frac{eV}{\Delta}\right) \frac{1}{\ln \tilde{r} - \ln[e^{(\ln(10)/20)(S_0 - S_{21})} - 1]}, \quad (7)$$

where  $\tilde{r} = \sqrt{\pi \Delta / (2k_B T)} R_0 / R_T$ . An estimate of  $R_0$  can be obtained from the measured  $dI/dV$  versus the bias  $V$ , because at  $|V| \rightarrow \infty$ ,  $dI/dV \rightarrow R_T^{-1}$ , the resistance of the tunnel junction. On the other hand, at low bias,  $R_0 dI/dV \ll 1$ . Combining these results, we have  $R_0/R_T \simeq 10^{\Delta S/20} - 1$ , where  $\Delta S = S_{21}(V \approx 0) - S_{21}(|V| \gg \Delta/e)$ .

In order to have a pure  $N$ - $I$ - $S$  configuration, the direct superconducting contact is placed 1  $\mu\text{m}$  away from the thermometer junction in sample B. In practice, this leads to a vanishing proximity effect at the thermometer junction. The transmission  $S_{21}$  as a function of voltage bias of the thermometer for a set of bath temperatures  $T_{\text{bath}}$  is presented in Fig. 3(a). In all these measurements, bath temperatures are obtained based on primary Coulomb blockade thermometer (CBT) [27]. Figure 3(b) shows the data points extracted from the transmission curves at fixed voltage biases for different bath temperatures. The solid lines show fits to the corresponding experimental data based on Eq. (7). It is clear that all the experimental sets match the calculated ones with  $\tilde{r}$  and  $S_0$  as fitting parameters. In these curves, the gap  $\Delta = 220$   $\mu\text{V}$  is determined independently by measuring the IV curves and, due to the exponential dependence  $\Delta(T)/\Delta(0) = 1 - \sqrt{2\pi k_B T / \Delta(0)} e^{-\Delta(0)/k_B T}$ , we may assume that  $\Delta$  has its low  $T$  value within 0.2% over the whole experimental range up to approximately 400 mK [28]. Furthermore, we ignore the logarithmic temperature dependence on  $\tilde{r}$  of the right-hand side of Eq. (7). The QP thermometer loses its sensitivity at low  $T$ , demonstrated by the vanishing responsivity  $\mathbb{R} \equiv |dS_{21}/dT|$ .

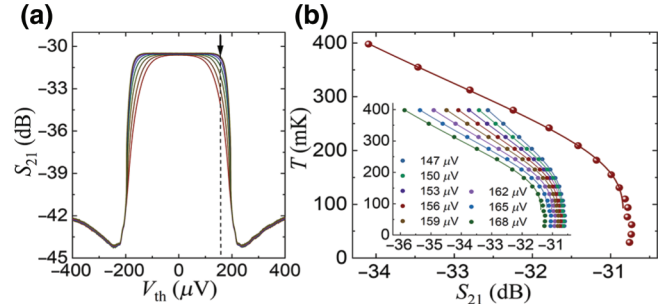


FIG. 3. Measured characteristics of the rf thermometer in the quasiparticle (QP) regime (sample B). (a) The transmission  $S_{21}$  as a function of the dc bias voltage  $V_{\text{th}}$ . The measurement is performed at temperatures 301, 263, 225, 182, 143, 113, 89, 68, 56, and 50 mK from bottom to top. (b) Temperature calibrations at  $V_{\text{th}} = 156$   $\mu\text{V}$  measured at  $-100$  dBm of the rf signal in the main panel and at various bias points in the inset. The lines are based on Eq. (7).

It is advantageous for calorimetry to work at as low a temperature as possible. This is because the energy resolution of an ideal calorimeter limited by fundamental thermal fluctuations is given by  $\delta\epsilon = \sqrt{k_BCT} \propto T^{3/2}$  [29]. Therefore, one would hope to have a sensitive and reliable thermometer down to the lowest temperatures reachable by a standard dilution refrigerator. For this purpose, we next present and analyze a different concept, which avoids the vanishing responsivity at low  $T$ .

#### IV. ZERO-BIAS-ANOMALY THERMOMETER

A zero-bias anomaly in tunnel junctions does appear due to numerous different effects: density of states in the conductors, magnetism in the electrodes, dynamic Coulomb effects, finite environment impedance, superconducting proximity effect, etc., as reviewed in the literature over the past decades [22,30–33]. Here, in sample A, we place the clean superconducting contact closer to the thermometer junction ( $d = 500$  nm). This gives the proximity effect to the normal metal with superconducting properties extending all the way to the position of the thermometer  $\mathfrak{N}-I-S$  junction. In this case, a zero-bias anomaly arises as shown in Fig. 4(a). This is to be compared to the measurement in the same setup in Fig. 3(a), where in sample B we observe no structure in the low-bias region.

Figure 4(b) exhibits transmission  $S_{21}$  results at different rf power levels in sample A. It is vivid that, because of the narrow ZBA feature, the result is sensitive to the applied power. This ZBA offers us a sensitive probe of temperature here down to the base temperature of the measurement (25 mK) as shown in Fig. 4(c), where temperature versus the zero-bias  $S_{21}$  is presented. This probe is nondissipative (zero bias) and sensitive (no saturation) at low temperatures, in contrast to the QP thermometer. It is worth pointing out that the responsivity  $\mathbb{R}$  of a ZBA thermometer at  $T < 200$  mK is approximately 0.06 dB/mK, which clearly exceeds  $\mathbb{R} \simeq 0.01$  dB/mK of the QP thermometer in the temperature range of its applicability. Temperature calibrations measured with different powers, shown in the inset of Fig. 4(c), demonstrate that measuring with a larger power ( $-120$ ,  $-125$  dBm) leads to saturation of  $S_{21}$  at low temperatures. One can also see that ZBA is composed of several peaks with the origin in the supercurrent and possibly in multiple Andreev reflection due to the relatively high transparency of the junction [34–37]. The backbending at  $T > 300$  mK is due to the QP current.

In order to compare different thermometers in sample A, we manipulate the electronic temperature  $T_e$  of the  $N$  island by applying a bias voltage  $V_{\text{inj}}$  across the auxiliary junction, denoted “injector” in Fig. 1(b) with tunnel resistance  $R_{\text{inj}} \simeq 50$  k $\Omega$ . The influence of this bias is the feature depicted in Fig. 5(a). In all curves, the electronic temperature drops at  $V_{\text{inj}} \sim \Delta/e$  due to the well-known quasiparticle cooling effect [38]. Operating the thermometer at

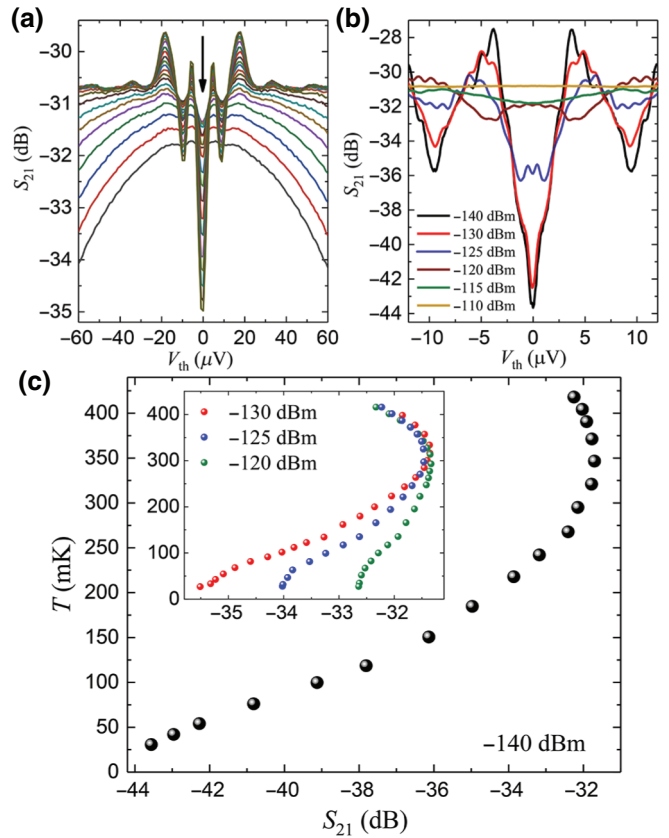


FIG. 4. The transmission of the proximitized junction of sample A in the ZBA regime,  $S_{21}$  versus  $V_{\text{th}}$ , for (a) a set of bath temperatures  $T_{\text{bath}}$  in the range of 27 to 398 mK and fixed power  $-130$  dBm and (b) a few power levels at  $T = 30$  mK. (c) Temperature calibration curves of the transmitted power at zero bias measured at  $-140$  dBm of the rf signal in the main panel and at different power levels  $-130$ ,  $-125$ , and  $-120$  dBm in its inset. The nonmonotonic order of the curves in panel (a) at zero bias with respect to the bath temperature corresponds to that in the inset of panel (c).

three different conditions, including zero with two different powers and several bias values as a QP thermometer, indicates close to identical temperatures over the whole  $V_{\text{inj}}$  bias range. In Fig. 5(b), we have collected measurements with different bias points  $V_{\text{th}}$  of the thermometers, while measuring the minimum temperatures  $T_{\text{min}}$  at  $V_{\text{inj}} \sim \Delta/e$  versus bath temperature  $T_{\text{bath}}$ . A QP thermometer at various bias points spans over the range from  $\gtrsim 100$  to 400 mK, whereas a ZBA thermometer can be used down to the minimum temperature of the cryostat in this experiment.

We observe that the measurements form a continuous set of data showing the optimum cooling around 200 mK. Based on the collapse of the different sets of data in Fig. 5, we conclude that all these thermometers measure, in a consistent way, the temperature of the electrons in the island.

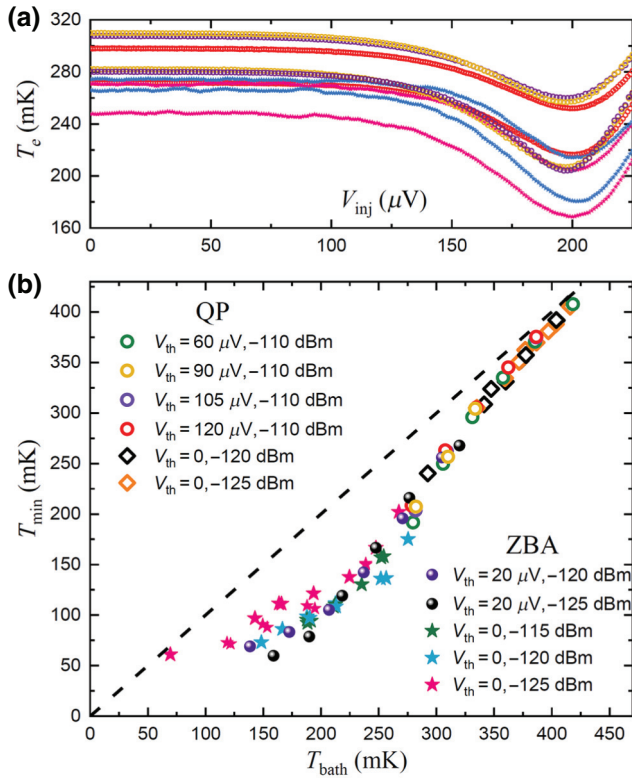


FIG. 5. Measurement of electron temperature  $T_e$  of the absorber under nonequilibrium conditions produced by applying voltage  $V_{\text{inj}}$  across the injector junction. (a) The voltage dependence of  $T_e$  demonstrates cooling, measured with different biasing and power levels of the thermometer. (b) Extracted minimum temperature of  $T_e$  as a function of bath temperature  $T_{\text{bath}}$ . The dashed line denotes  $T_{\min} = T_{\text{bath}}$ .

## V. DISCUSSION OF ZBA CALORIMETER

Here, we discuss the feasibility of measuring single energy quanta with a ZBA thermometer and compare its performance to the QP method. We show quantitatively that the main advantages of ZBA-based calorimetry are its low operation temperature and ultralow power dissipation. The challenge, on the other hand, is that only low-input power levels are feasible as the ZBA peak is very narrow in  $V_{\text{th}}$ .

*Noninvasiveness of ZBA.*—An important key for a nanocalorimeter, in order to be able to detect single quanta like photons with an energy of approximately  $100 \mu\text{V}$ , is to be noninvasive [39]. Using Eq. (6) and considering  $\Delta/e = 200 \mu\text{V}$  for the superconducting gap of Al,  $V = 0.8\Delta/e$ , and  $T = 130 \text{ mK}$  as parameters for sample B, the QP thermometer injects approximately  $15 \text{ aW}$  of heat. On the other hand, the corresponding power for ZBA thermometer in sample A [using Eq. (4) and  $-140 \text{ dBm}$  for applied rf power] is approximately  $4 \text{ zW}$  at  $25 \text{ mK}$ , i.e., approximately  $10^6$  times less than in the QP thermometer.

*Sensitivity at low  $T$ .*—We start by estimating the required noise-equivalent temperature  $\sqrt{S_T}$ , which we denote  $\text{NET}_{\text{req}}$  in  $\mu\text{K}/\sqrt{\text{Hz}}$  [2]. For energy, we choose  $\delta\epsilon_e = 2.5 \text{ K} \times k_B$  for measurements described in [39] to detect an electron tunneling over the superconducting gap of Al and  $\delta\epsilon_{\text{ph}} = 1 \text{ K} \times k_B$  for a 20-GHz single microwave photon. Figures 6(a) and 6(b) demonstrate the feasibility of measuring the energy deposited by single electrons and single microwave photons by the envisioned calorimeter with a copper absorber. Both the panels present various predicted  $\text{NET}$  values as functions of the operation temperature for two different volumes of the absorber,  $0.0025 \mu\text{m}^3$ , which is the current sample A, and  $0.0005 \mu\text{m}^3$  that represents a technically realistic tiny absorber (called sample Opt), respectively. In this figure, the black lines in both panels Figs. 6(a) and 6(b) represent fundamental temperature fluctuations  $\text{NET}_0 = \sqrt{S_Q/G_{\text{th}}^2} = \sqrt{2k_B/(5\Sigma\mathcal{V})}T^{-1}$ , where, according

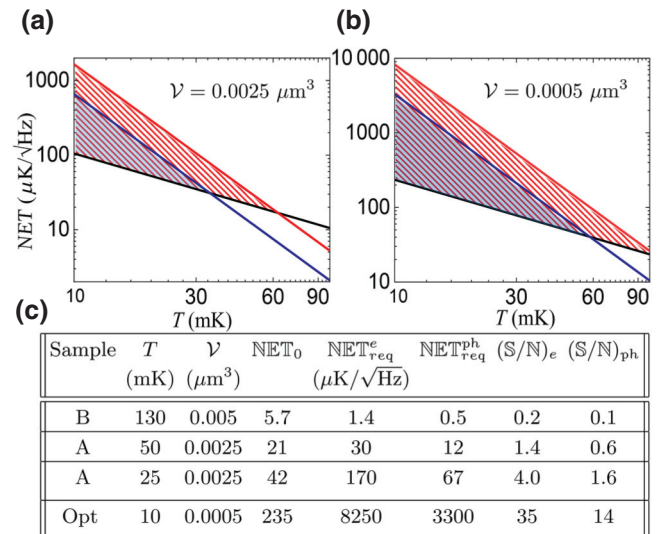


FIG. 6. Requirements for detecting the heat produced by single-electron  $\delta\epsilon_e = 2.5 \text{ K} \times k_B$  and single-photon  $\delta\epsilon_{\text{ph}} = 1 \text{ K} \times k_B$  quanta. Dependence of various noise-equivalent temperatures  $\text{NET}$  on bath temperature  $T_{\text{bath}}$  for two different volumes of copper absorber, (a)  $0.0025 \mu\text{m}^3$  and (b)  $0.0005 \mu\text{m}^3$ . In both panels, the black lines demonstrate the fundamental temperature fluctuations  $\text{NET}_0$ , red lines show the required noise-equivalent temperature for electrons  $\text{NET}_{\text{req}}^e$ , and blue lines for photons  $\text{NET}_{\text{req}}^{\text{ph}}$ . The shaded areas indicate the feasible regimes, where the corresponding quanta can be observed. In panel (c), we present concrete examples referring to the samples B, A, and Opt that have a small volume yet are experimentally feasible. QP and ZBA thermometry are used for samples B and A, respectively, at the minimum temperature  $130 \text{ mK}$  for QP and two different temperatures for ZBA. The last two columns give the corresponding signal-to-noise ratio for detecting electrons  $(\text{S}/\text{N})_e$  and photons  $(\text{S}/\text{N})_{\text{ph}}$ . The parameters used for evaluating the present results in panels (a)–(c) are  $\Sigma = 2 \times 10^9 \text{ WK}^{-5} \text{ m}^{-3}$  and  $\gamma = 70 \text{ JK}^{-2} \text{ m}^{-3}$ .

to the fluctuation dissipation theorem,  $S_Q = 2k_B T^2 G_{\text{th}}$  is the heat current noise in equilibrium. The two other lines denote the required noise-equivalent temperature  $\text{NET}_{\text{req}}^i = \delta\epsilon_i / (\mathcal{V}\sqrt{5\gamma\Sigma})T^{-5/2}$  for  $i = e, \text{ph}$ , to observe quanta of energy for electrons (red lines) and photons (blue lines). For our estimations, we use the well-known expressions for the thermal conductance to the phonon bath  $G_{\text{th}} = 5\Sigma\mathcal{V}T^4$  [40] and  $C = \gamma\mathcal{V}T$  for the heat capacity of the normal metal. Here,  $\Sigma$  denotes the electron-phonon constant [38],  $\mathcal{V}$  the volume of the island, and  $\gamma$  refers to the Sommerfeld constant for electrons in metal. The shaded areas delineate the favorable regimes for detecting these particles. The upper boundary is given by the required  $\text{NET}_{\text{req}}^i$  and the lower bound (black line) represents the fundamental temperature fluctuations  $\text{NET}_0$ .

The table presented in Fig. 6(c) shows examples of these estimates under four different conditions. The first row presents sample B with QP thermometry around its lowest operation temperature (130 mK). The estimates for the ZBA thermometer of sample A at two different temperatures (50 and 25 mK) are given in the second and third rows, respectively. Here, in the absence of precise temperature calibration for ZBA, the two rows represent the conservative and optimistic estimates of the actual base temperature using ZBA. The fourth row indicates a further optimized sample, Opt, with experimentally feasible target parameters. The fifth and sixth columns in the table,  $\text{NET}_{\text{req}}^e$  and  $\text{NET}_{\text{req}}^{\text{ph}}$ , demonstrate that it is next to impossible to detect a single electron  $e$  or photon  $\text{ph}$  with a QP thermometer. Yet, using ZBA at lower  $T$ , the requirement for  $\text{NET}$  is relaxed by one to two orders of magnitude. The typical  $\text{NET}$  in the present measurement is around  $30 \mu\text{K}/\sqrt{\text{Hz}}$  based on the ZBA thermometer (including the amplifier noise). Thus, the current  $\text{NET}$  is just about to be sufficient to detect  $2.5 \text{ K} \times k_B$ . In the last two columns, we present the expected signal-to-noise ratio ( $\text{S/N}$ ) $_i$  for different quanta,  $i = e, \text{ph}$ , demonstrating the possibility of detecting them ( $\text{S/N} > 1$ ) by ZBA at low temperatures and with small absorber. Technically, the numbers are obtained as the ratio  $\text{NET}_{\text{req}}^i/\text{NET}_0$  at the corresponding conditions. We then observe that the  $\text{S/N}$  ratio falls unfortunately far below unity for the QP thermometer at all experimental conditions presented. On the contrary, the numbers for ZBA are far more encouraging ( $\text{S/N} > 10$ ), especially at the lowest temperatures with an optimized system.

Finally, we comment briefly on how to optimize the ZBA thermometer in the future. The critical current  $I_c$  of the  $\text{M}-\text{I}-\text{S}$  junction and the zero-bias conductance are expected to increase rapidly when the distance of the clean contact  $d$  from the junction decreases [28,41]. Therefore, higher responsivity is expected for smaller values of  $d$ : in practice,  $d$  can be decreased down to approximately 50 nm from the current 500 nm, potentially leading to about a one-order-of-magnitude increase in responsivity.

Moreover, the frequency shift of the resonance due to Josephson inductance will also be enhanced in this case, giving an extra boost in the sensitivity of the ZBA thermometer.

In conclusion, we demonstrate a fast noninvasive thermometer with high responsivity down to approximately 25-mK temperature based on superconducting-proximity-induced ZBA, outperforming the standard QP thermometer, both in sensitivity and dissipated power. With a lower but still realistic operation temperature of approximately 10 mK and the proposed improvements in design, the ZBA calorimeter can detect single microwave photons.

## ACKNOWLEDGMENTS

We acknowledge J. T. Peltonen and E. T. Mannila for technical support and F. Brange, P. Samuelsson, D. Golubev, A. Mel'nikov, O.-P. Saira, K. L. Viisanen, W. Belzig, I. Khaymovich, and P. Muratore-Ginanneschi for useful discussions. We acknowledge the facilities and technical support of Otaniemi Research Infrastructure for Micro and Nanotechnologies (OtaNano). This work is funded through Academy of Finland Grants No. 297240, No. 312057, and No. 303677 and from the European Union's Horizon 2020 research and innovation program under the European Research Council (ERC) program and Marie Skłodowska-Curie actions (Grants No. 742559 and No. 766025).

- 
- [1] S. P. Langley, The bolometer, *Nature* **57**, 620 (1898).
  - [2] P. L. Richards, Bolometers for infrared and millimeter waves, *J. Appl. Phys.* **76**, 1 (1994).
  - [3] Christian Enss (Ed), *Cryogenic Particle Detection* (Springer-Verlag, Berlin, Heidelberg, 2005).
  - [4] D. McCammon, S. H. Moseley, J. C. Mather, and R. F. Mushotzky, Experimental tests of a single-photon calorimeter for x-ray spectroscopy, *J. Appl. Phys.* **56**, 1263 (1984).
  - [5] J. P. Pekola, P. Solinas, A. Shnirman, and D. V. Averin, Calorimetric measurement of work in a quantum system, *New J. Phys.* **15**, 115006 (2013).
  - [6] Kunihiro Inomata, Zhirong Lin, Kazuki Koshino, William D. Oliver, Jaw-Shen Tsai, Tsuyoshi Yamamoto, and Yasunobu Nakamura, Single microwave-photon detector using an artificial  $\Lambda$ -type three-level system, *Nat. Commun.* **7**, 12303 (2016).
  - [7] G. Oelsner, C. K. Andersen, M. Rehák, M. Schmelz, S. Anders, M. Grajcar, U. Hübner, K. Mølmer, and E. Il'ichev, Detection of Weak Microwave Fields with an Under-damped Josephson Junction, *Phys. Rev. Appl.* **7**, 014012 (2017).
  - [8] K. L. Viisanen and J. P. Pekola, Anomalous electronic heat capacity of copper nanowires at sub-kelvin temperatures, *Phys. Rev. B* **97**, 115422 (2018).
  - [9] D. R. Schmidt, C. S. Yung, and A. N. Cleland, Nanoscale radio-frequency thermometry, *Appl. Phys. Lett.* **83**, 1002 (2003).

- [10] Francesco Giazotto and María José Martínez-Pérez, The Josephson heat interferometer, *Nature* **492**, 401 (2012).
- [11] S. Gasparinetti, K. L. Viisanen, O.-P. Saira, T. Faivre, M. Arzeo, M. Meschke, and J. P. Pekola, Fast Electron Thermometry Towards Ultra-Sensitive Calorimetric Detection, *Phys. Rev. Appl.* **3**, 014007 (2015).
- [12] J. Govenius, R. E. Lake, K. Y. Tan, and M. Möttönen, Detection of Zeptojoule Microwave Pulses Using Electrothermal Feedback in Proximity-Induced Josephson Junctions, *Phys. Rev. Lett.* **117**, 030802 (2016).
- [13] L. B. Wang, O.-P. Saira, and J. P. Pekola, Fast thermometry with a proximity Josephson junction, *Appl. Phys. Lett.* **112**, 013105 (2018).
- [14] Dorri Halbertal, Moshe Ben Shalom, Aviram Uri, Kousik Bagani, Alexander Y. Meltzer, Ido Marcus, Yuri Myasoev, John Birkbeck, Leonid S. Levitov, Andre K. Geim, and Eli Zeldov, Imaging resonant dissipation from individual atomic defects in graphene, *Science* **358**, 1303 (2017).
- [15] Z. Iftikhar, A. Anthore, S. Jezouin, F. D. Parmentier, Y. Jin, A. Cavanna, A. Ouerghi, U. Gennser, and F. Pierre, Primary thermometry triad at 6 mK in mesoscopic circuits, *Nat. Commun.* **7**, 12908 (2016).
- [16] Mitali Banerjee, Moty Heiblum, Amir Rosenblatt, Yuval Oreg, Dima E. Feldman, Ady Stern, and Vladimir Umansky, Observed quantization of anyonic heat flow, *Nature* **545**, 22052 (2017).
- [17] M. Foltyn and M. Zgirski, Gambling with Superconducting Fluctuations, *Phys. Rev. Appl.* **4**, 024002 (2015).
- [18] Federico Paolucci, Giorgio De Simoni, Elia Strambini, y Paolo Solinas, and Francesco Giazotto, Ultra-efficient superconducting Dayem bridge field-effect transistor, arXiv:1803.04925 (2018).
- [19] O.-P. Saira, M. Zgirski, K. L. Viisanen, D. S. Golubev, and J. P. Pekola, Dispersive Thermometry with a Josephson Junction Coupled to a Resonator, *Phys. Rev. Appl.* **6**, 024005 (2016).
- [20] B. Pannetier and H. Courtois, Andreev reflection and proximity effect, *J. Low Temp. Phys.* **118**, 599 (2000).
- [21] S. Gueron, H. Pothier, Norman O. Birge, D. Esteve, and M. H. Devoret, Superconducting Proximity Effect Probed on a Mesoscopic Length Scale, *Phys. Rev. Lett.* **77**, 3025 (1996).
- [22] A. Kastalsky, A. W. Kleinsasser, L. H. Greene, R. Bhat, F. P. Milliken, and J. P. Harbison, Observation of Pair Currents in Superconductor-Semiconductor Contacts, *Phys. Rev. Lett.* **67**, 3026 (1991).
- [23] H. A. Nilsson, P. Samuelsson, P. Caroff, and H. Q. Xu, Supercurrent and multiple Andreev reflections in an InSb nanowire Josephson junction, *Nano Lett.* **12**, 228 (2012).
- [24] Alberto Ronzani, Carles Altimiras, and Francesco Giazotto, Highly Sensitive Superconducting Quantum-Interference Proximity Transistor, *Phys. Rev. Appl.* **2**, 024005 (2014).
- [25] M. Nahum and John M. Martinis, Ultrasensitive-hot-electron microbolometer, *Appl. Phys. Lett.* **63**, 3075 (1993).
- [26] A. V. Gordeeva, V. O. Zbrozhek, A. L. Pankratov, L. S. Revin, V. A. Shamporov, A. A. Gunbina, and L. S. Kuzmin, Observation of photon noise by cold-electron bolometers, *Appl. Phys. Lett.* **110**, 162603 (2017).
- [27] J. P. Pekola, K. P. Hirvi, J. P. Kauppinen, and M. A. Paalanen, Thermometry by Arrays of Tunnel Junctions, *Phys. Rev. Lett.* **73**, 2903 (1994).
- [28] M. Tinkham, *Introduction to Superconductivity* (Dover, New York, 1996), 2nd ed.
- [29] E. M. Lifshitz and L. P. Pitaevskii, *Statistical Physics, Part I* (Pergamon Press, Oxford, 1980), 3rd ed.
- [30] Elias Burstein and Stig Lundqvist, *Tunneling Phenomena in Solids* (Plenum Press, New York, 1969).
- [31] J. M. Rowell and L. Y. L. Shen, Zero-Bias Anomalies in Normal Metal Tunnel Junctions, *Phys. Rev. Lett.* **17**, 15 (1966).
- [32] T. Holst, D. Esteve, C. Urbina, and M. H. Devoret, Effect of a Transmission Line Resonator on a Small Capacitance Tunnel Junction, *Phys. Rev. Lett.* **73**, 3455 (1994).
- [33] V. Mourik, K. Zuo, S. M. Frolov, S. R. Plissard, E. P. A. M. Bakkers, and L. P. Kouwenhoven, Signatures of majorana fermions in hybrid superconductor-semiconductor nanowire devices, *Science* **336**, 1003 (2012).
- [34] Athanassios Bardas and Dmitri V. Averin, Electron transport in mesoscopic disordered superconductor normal-metal superconductor junctions, *Phys. Rev. B* **56**, R8518 (1997).
- [35] E. Scheer, P. Joyez, D. Esteve, C. Urbina, and M. H. Devoret, Conduction Channel Transmissions of Atomic-Size Aluminum Contacts, *Phys. Rev. Lett.* **78**, 3535 (1997).
- [36] J. C. Cuevas, J. Hammer, J. Kopu, J. K. Viljas, and M. Eschrig, Proximity effect and multiple Andreev reflections in diffusive superconductor-normal-metal-superconductor junctions, *Phys. Rev. B* **73**, 184505 (2006).
- [37] T. M. Klapwijk, G. E. Blonder, and M. Tinkham, Explanation of subharmonic energy gap structure in superconducting contacts, *Phys. B & C* **109**, 1657 (1982).
- [38] Francesco Giazotto, Tero T. Heikkilä, Arttu Luukanen, Alexander M. Savin, and Jukka P. Pekola, Opportunities for mesoscopics in thermometry and refrigeration: Physics and applications, *Rev. Mod. Phys.* **78**, 217 (2006).
- [39] F. Brange, P. Samuelsson, B. Karimi, and J. P. Pekola, Nanoscale quantum calorimetry with electronic temperature fluctuations, *Phys. Rev. B* **98**, 205414 (2018).
- [40] M. L. Roukes, M. R. Freeman, R. S. Germain, R. C. Richardson, and M. B. Ketchen, Hot Electrons and Energy Transport in Metals at Millikelvin Temperatures, *Phys. Rev. Lett.* **55**, 422 (1985).
- [41] P. Dubos, H. Courtois, B. Pannetier, F. K. Wilhelm, A. D. Zaikin, and G. Schön, Josephson critical current in a long mesoscopic S-N-S junction, *Phys. Rev. B* **63**, 064502 (2001).